INTERNATIONAL JOURNAL OF
Applied Glass
SCIENCE

ORIGINALA ARTICLE

Melt property variation in GeSe₂-As₂Se₃-PbSe glass ceramics for infrared gradient refractive index (GRIN) applications

Anupama Yadav[1] (iD) | Andrew Buff[1] | Myungkoo Kang[1] | Laura Sisken[1] |
Charmayne Smith[1] | Jason Lonergan[1] | Cesar Blanco[1] | Michael Antia[1] | Megan Driggers[2] |
Andrew Kirk[2] | Clara Rivero-Baleine[2] | Theresa Mayer[3] | Andrew Swisher[4] |
Alexej Pogrebnyakov[4] | AR Hilton Jr[5] | Greg Whaley[5] | Thomas J. Loretz[6] |
Anthony Yee[7] | Greg Schmidt[7] | Duncan T. Moore[7] | Kathleen A. Richardson[1]

[1]College of Optics and Photonics, CREOL, University of Central Florida, Orlando, Florida

[2]Lockheed Martin Corporation, Orlando, Florida

[3]Virginia Polytechnic Institute and State University, Blacksburg, Virginia

[4]Department of Electrical Engineering, The Pennsylvania State University, University Park, Pittsburgh

[5]Amorphous Materials Inc., Garland, Texas

[6]Computer Engineering Service, Waxhaw, North Carolina

[7]Institute of Optics, University of Rochester, Rochester, New York

Correspondence
Anupama Yadav and Kathleen A. Richardson, College of Optics and Photonics, CREOL, University of Central Florida, Orlando, FL.
Emails: yadav.anupama@knights.ucf.edu (A. Y); kcr@creol.ucf.edu (K. A. R.)

Abstract

Melt size-dependent physical property variation is examined in a multicomponent GeSe₂-As₂Se₃-PbSe chalcogenide glass developed for gradient refractive index applications. The impact of melting conditions on small (40 g) prototype laboratory-scale melts extended to commercially-relevant melt sizes (1.325 kg) have been studied and the role of thermal history variation on physical and optical property evolution in parent glass, the glass' crystallization behavior and postheat-treated glass ceramics, is quantified. As-melted glass morphology, optical homogeneity and heat treatment-induced microstructure following a fixed, two-step nucleation and growth protocol exhibit marked variation with melt size. These attributes are shown to impact crystallization behavior (growth rates, resulting crystalline phase formation) and induced effective refractive index change, n_{eff}, in the resulting optical nanocomposite. The magnitude of these changes is discussed based on thermal history related melt conditions.

KEYWORDS
chalcogenide glasses, crystallization, glass-ceramics, gradient refractive index, infrared, liquid-liquid phase separation

1 | INTRODUCTION

Rapid evolution of infrared (IR) technology is making it possible to employ infrared optical components for low-cost consumer sensing and security applications, as well as extreme-performance applications in defense. The unique properties and functionalities of chalcogenide glasses (ChGs) are well suited for applications spanning the short-wave (SWIR), mid-wave (MWIR) and long-wave IR (LWIR) spectral regimes. These amorphous glasses exhibit low phonon energies, high refractive indices, high optical nonlinearity, transparency from the visible to the infrared wavelengths and low dispersion.[1–5] ChGs can easily be molded into lenses or drawn into fibers.[6,7] By varying

elemental composition, optical and thermal properties of multicomponent ChGs can be tailored to provide optical and systems designers and manufacturers additional degrees of freedom than those possible using crystalline IR materials.

The demand for larger volumes of low-cost IR optical elements that perform across multiple IR bands (eg, MWIR + LWIR or SWIR + MWIR) make ChGs attractive candidate materials as thermal imaging and sensing technologies have become affordable to the consumer. Typically, optical devices require the use of multiple lenses to form a high quality image with low aberrations. Such designs may have structural limitations related to the shape and number of the required lenses. Gradient refractive index (GRIN) materials are ideal for optical elements where a gradual variation in the refractive index is used to manipulate light.[8–11] This continuous variation in index not only allows an additional degree of freedom that can be used for high focusing power or aberration correction, but also provides unique and tailorable dispersion characteristics not possible with homogenous optical materials.[12] Implementation of GRIN optical designs can enable cost effectiveness through the manufacturing of fewer optical elements but more importantly, reduces the number of coated surfaces and reflections while improving transmission and spectral range performance.

Currently deployed technologies for producing GRIN profiles have largely focused on solutions for the visible. These methods include neutron irradiation, chemical vapor deposition, ion exchange, and multilayer lamination techniques of polymers or glass, which are usually not sufficient for advanced optical designs because they are often produce optics that are limited by loss or the magnitude of a finite refractive index change (Δn).[13–16] Two teams funded through DARPA's M-GRIN program have recently examined GRIN materials for the IR. Naval Research Laboratory (NRL) has developed multiple, single glass compositions and exploited a fusion bonding method on ChG wafers employing interdiffusion of glass constituents. This results in a gradual, diffusion-limited index step where end points are defined by the number of wafers and their starting indices.[17,18] Within the mid-wave infrared (MWIR), it has also been demonstrated that a combination of zinc sulfide (ZnS) and zinc selenide (ZnSe) grown using a co-deposition method to realize ZnSSe via Chemical Vapor Deposition (CVD) is also capable of forming a GRIN profile.[19]

The candidate ChG composition evaluated in this study was developed in a partnership between the University of Central Florida (UCF), Penn State, and Lockheed Martin Corporation (LMCO) researchers,[20] and offers the potential of creating an arbitrary GRIN profile through the spatial control of nuclei formation followed by a secondary growth step resulting in a multiphase (nanocrystallite + glass) glass-ceramic. Here, the effective refractive index variation, Δn_{eff} of the resulting nanocomposite is proportional to the volume fraction of the crystalline phase within the parent glass, and their respective refractive indices. The GRIN profile is produced by forming a secondary crystalline phase with higher (or lower) index than the parent glass. Growing a controlled number density of small (<100 nm) single-phase crystallites in a glass matrix is very challenging. Uncontrolled 'spontaneous' crystallization can lead to large crystallites of multiple phases imparting absorption or scattering loss within the target infrared transmission window.[21,22] If the crystal sizes can be kept well below approximately one-half to one-tenth of the wavelength range of use, light scattering within the material can be minimized. In this work, crystallites are produced via controlled crystallization of the glass using a two-step nucleation and growth heat treatment. Extensive evaluation of the times and temperatures optimal for this two-stage protocol is discussed in detail in reference.[23] The goal of the present effort has been to form a controlled volume fraction of crystals with a higher refractive index than the parent glass and to assess the resulting glass-ceramic's properties for a fixed parent glass composition.

In addition to understanding the methodology required to induce controlled crystallization in the glass, the influence of melt size on the properties of the resultant glass-ceramic is a topic of intense scientific and engineering importance. Most "academic" investigations involve small melt sizes with melting protocols far different from those used by commercial glass manufacturers preparing larger melt volumes with higher levels of optical homogeneity. For materials to be considered suitable for use in current and future optical systems, the impact of melt-size thermal history on the base glass' optical properties, as well as its subsequent behavior when crystal phase formation occurs in the parent glass, must be understood. This is especially important if lab-scale prototype glass melts (<100 g in size) are transitioned to larger scale melts (>1 kg). An understanding of the difference between properties of the laboratory-scale glass melt and the subsequent glass' properties upon scale-up is desired to show that these compositions can be commercialized. Such a systematic study is often not reported as it is a source of proprietary commercial "know-how", not frequently discussed in published literature. This paper reports such a systematic study.

It is commonly understood that as the volume (size) of a glass melt increases, it becomes more difficult to extract heat from the melt. This reduction in the melt cooling rate can impart adverse effects on glass homogeneity and crystallization stability of the melt if a prescribed process is not followed. This can be even more pronounced in glass systems such as ChGs, which are well known to exhibit

liquid-liquid phase separation (LLPS).[24] The cooling rate of a glass melt can have significant impact on the properties of the glass including its glass transition temperature (T_g), crystallization temperature (T_x), thermal stability ($\Delta T = T_x - T_g$), density, and refractive index.[25] Additionally, slow cooling rates may lead to an increase in number of as-quenched nuclei or the extent of phase separation; both of these attributes make use in optical applications or subsequent processing (ie, to a glass-ceramic) difficult. While slow cooling rates may have negative effects on the glass by producing these inhomogeneities, such slow cooling is required for yielding (high) refractive index optical homogeneity. Index inhomogeneity typically occurs from compositional, and thereby density fluctuations within the melt that result in striae upon cooling which degrade transmission through the optical component. Striae are typically "born" upon cooling from the melting region at high temperatures when the molten glass is quite turbulent due to convective movement within the melt. If the melt is rapidly quenched, such turbulent flow is "frozen" into the glass, resulting in bubbles or density gradients. Controlled cooling through the transition region allows the melt enough time to relax so that the fluctuations are not "frozen" into the glass. Other optical inhomogeneities in the glass which can result in stress-induced birefringence may arise as the glass passes through the transition region, near T_g. As the outside of the glass melt solidifies before the inside, the contraction during solidification can cause striations in the melt which cannot be removed with annealing thus remaining permanently frozen in the glass network. These facts are especially important when making direct comparisons of a fixed composition across varying melt sizes. Hence, as this effort has transitioned a candidate GRIN material from lab-scale to prototype industry scale size, a review of how optical and physical property variation "scales" is warranted.

The work reported in this paper examines the role of phase separation morphology on crystallization behavior and postheat treatment properties in a phase separated quaternary chalcogenide glass composition in the $20GeSe_2$-$60As_2Se_3$-$20PbSe$ (20 PbSe) system. The attributes of this glass are part of a series of glasses (with varying PbSe content) that have been previously reported, for small, 40 g melts.[26] Here, we focus on one composition to systematically evaluate important property and performance variations that result from melt size scale-up (from 40 g melts to 1325 g melts) that can affect the material's suitability for use as a GRIN material in IR optical systems. The microstructure of the crystalline phases created following a fixed nucleation and growth heat treatment protocol of the base glass is presented, and the variation in properties of this postheat-treated glass-ceramic material is reported. The postheat-treated 20 PbSe glass-ceramic has been shown to exhibit good transparency in the mid-infrared with a narrow size distribution of crystallized phases. Presented are the details of the glass' droplet size and total droplet volume fraction, as well as the glass-ceramic's crystal phases, refractive index change and optical transparency and how each varies with the parent glass' melt size. The findings of this study shows that the crystallization behavior of varying parent glass morphology can be controlled to realize good optical quality nanocomposites despite variations of property attributes with melt size.

2 | EXPERIMENTAL PROCEDURE

Small batches of 40 and 150 g of $20GeSe_2$-$60As_2Se_3$-$20PbSe$ (20 PbSe) bulk glasses were prepared using conventional melt-quenching technique in the *Glass Processing and Characterization Laboratory* (GPCL) at the University of Central Florida (UCF). All glasses were prepared using high purity raw materials (metals basis) from Alfa Aesar: Selenium (99.999%), Germanium (99.999%), Arsenic (99.999%), and Lead (99.999%). Elemental starting materials were weighed and batched in a nitrogen purged, MBraun Labmaster 130 glove box. The weighed batch was loaded into cleaned fused quartz tubes (either 10 or 30 mm in diameter) and sealed under vacuum using a methane-oxygen torch to form sealed ampoules. All UCF batches were melted in a rocking furnace overnight at a melting temperature of $T_m = 850°C$. After the overnight rocking temperature, the furnace was then cooled to the quench temperature, $T_Q = 650°C$, prior to removal from the furnace for quenching using compressed air flowing over the ampoule. The cooling rate for this quench method is estimated to be ~120°C/min. To minimize any quench-related stress, the prepared glasses were annealed at 177°C for 2 hours. The annealed glass rods were cut into slices of thickness ~2.5 mm using a slow speed saw. For optical characterization, slices were ground and polished by hand on both sides using SiC paper with a final 0.05 μm Al_2O_3 slurry polishing step.

Working with our commercial partner, Amorphous Materials, Inc., (AMI), efforts to scale up the 20 PbSe composition were undertaken. Using proprietary, test-melting protocols, similar to those employed for other AMI commercial compositions, exploratory 500 g and 1325 g melts of the 20 PbSe composition were produced from elemental starting materials. AMI melts were either in the form of semi-elliptical cylinders (cast horizontally, within a round quartz tube, major radius ~27 mm; minor radius ~10 mm) or as ~200 mm (8") diameter plates (7 mm thick). These geometries were selected to maximize cooling rate (volume of melt in contact with the glass surface exposed to air for cooling). Both the 500 g and 1325 g test

melts were melted at 850°C. The 500 g melt was quenched from 500°C, while the 1325 g melt was quenched from 525°C. Both were cooled to 190°C as quickly as available air-convection techniques allowed, and then annealed.

The morphology, chemical composition, and microstructure of the base and heat-treated glasses were investigated using transmission electron microscopy (TEM). Glasses were ground into powder specimens, and dropped onto lacey carbon grids. Bright field (BF) TEM images, selected area electron diffraction (SAED) patterns, and X-ray energy dispersive spectroscopy (XEDS) images in a scanning transmission electron microscopy (STEM) mode were collected using a FEI Tecnai F30 TEM with an electron beam acceleration voltage of 200 kV.

Thermal studies were performed in a Netzsch DSC 204 F1 Phoenix Differential Scanning Calorimeter (DSC), using a constant sample size (20 ± 2.5 mg) of glass (particle size < 125 μm) and an empty aluminum pan as a reference. Initially, a DSC run was performed on the base glass at a base heating rate of 10°C/min to determine the characteristic glass transition (T_g) and crystallization (T_x) temperatures. DSC was also used to create nucleation-like and growth-like curves by analyzing curves after isothermal holds in the DSC following methods presented in [27,28] and discussed in detail for this 20 PbSe glass, in reference.[23]

Nucleation and growth curves were used to develop heat treatment protocols for bulk glass samples to form optical glass-ceramic nanocomposites. Polished specimens underwent a two-step heat treatment in an open-air electrical furnace for fixed nucleation and growth times and temperatures. All 20 PbSe glasses were nucleated at 220°C for 2 hours followed by a growth heat treatment at either 250, 260 or 270°C for 30 minutes. Physical properties (microhardness and density) were measured on the glasses before heat treatment, after nucleation heat treatment, and after growth heat treatment steps in order to characterize the effect of the crystallization process on properties. These data while useful to make melt-size, structure property comparisons, are not discussed in detail here but in the work of Buff[23]

Fourier Transform Infrared (FTIR) Spectroscopy was employed to measure the transmission of polished samples. Two separate Perkin Elmer FTIR systems were used. The Frontier FT-NIR model measures the transmission from 0.64-5 μm, while the Frontier Optica model measures transmission from 2-22 μm. The resolution of these systems is between ±1%. Using refractive index data at key wavelengths is of interest, the transmission curves were corrected for Fresnel losses.

Refractive index was measured before and after heat treatment on glass/glass-ceramic samples, using a Metricon Inc. prism coupler (2010 Metricon Corporation, Pennington, NJ, USA) modified to measure the index of bulk and thin film samples in the infrared. Specifics on the system modification and basic principles of its use and measurements on other chalcogenide glasses can be found in works by Carlie et al., Qiao et al., and Gleason et al.[29–31] Ten measurements were performed on each sample with an error of ± 0.0005 for measurements at λ = 4.515 μm. Two different prisms were used depending on the index of the sample. The lower index samples (index range at 4.515 μm ~2.05-3.05) were measured using an undoped, single-crystal Ge prism. The higher index samples (index range ~2.95-3.35) were measured using an undoped, single-crystal Si prism. A crystalline reference material (ZnSe) of known index was used as a calibration standard.

The internal homogeneity of the as-melted glasses was characterized using a FLIR infrared camera (to probe gross artifacts and striae) and IR interferometers (to quantify refractive index uniformity) in polished melt samples. Of special interest was the magnitude of such features and variation with melt size. Refractive index uniformity measurements at the University of Rochester were performed on a Mach-Zehnder interferometer at 4.5905 μm. The absolute refractive index at 4.5905 μm was measured, using a Sagnac interferometer. The index of refraction measured, using the Sagnac Interferometer has an accuracy and resolution on the order of 10^{-4}. A detailed summary of the technique can be found in reference [32] and is presented for GAP-Se glasses in reference [23] The Mach-Zehnder interferometer measures the deviation of the beam as it passes through the sample at different angles. These deviation measurements are then used to calculate the change in the refractive index, Δn.[33] Sources of error for these measurements come from poor surface quality of the test specimen, nonparallel sides, and severe internal striae as observed by imaging with a FLIR camera or interferometry.

X-ray diffraction (XRD) was performed on the PANalytical Empyrean system using a Cu K-alpha radiation source (λ = 0.154 nm) in a 2θ range from 10 to 70°. Measurements were performed on the base glass and on post-heat-treated samples to confirm the amorphous nature of the base glass and to identify and quantify crystalline phases formed in the heat-treated glass-ceramic.

3 | RESULTS AND DISCUSSION

3.1 | Glass properties as a function of melt size

Figure 1A-C shows XEDS compositional line scans across the droplet and matrix phase boundaries for selected 40, 500 and 1325 g melts of the parent 20 PbSe base glass composition. As discussed in Yadav et al.,[26] liquid-liquid phase separation (LLPS) in the glass results in the precipitation of droplets in the matrix of the melt/quenched GAP-
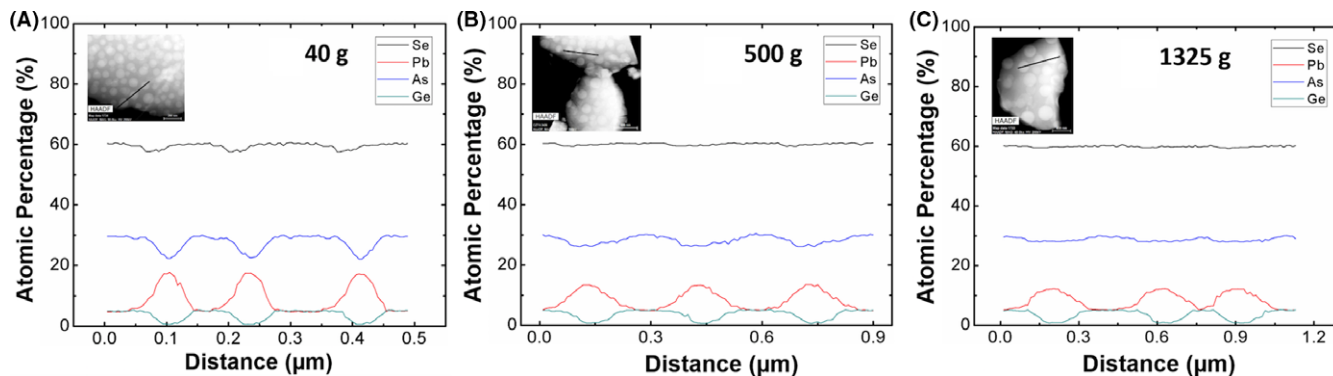
FIGURE 1 XEDS line scan for (A) 40 g, (B) 500 g and (C) 1325 g melts across the droplet-matrix phase boundaries for the base compositions (inset shows the TEM images for the corresponding composition). Note that the scale lengths required to measure across three droplets varies with melt size, consistent with the droplet size variation discussed below

Se glass. Electron diffraction confirmed that both droplet and matrix phases remain amorphous in all specimens with no evidence of crystallization. While EDS of the three melt specimens show identical compositional features for the four elements that comprise the $20GeSe_2$-$60As_2Se_3$-$20PbSe$ (20 PbSe) glass, only the Pb component shows any preference for phase segregation in the XEDS analysis performed on TEM images across multiple droplets within the phase separated morphology. Figure 1A-C show the quantitative compositional information of the droplet and matrix for the different melt size glasses. The XEDS line scans of the 20 PbSe glass show that the Pb is present throughout the sample but is much higher in content in the droplet phase as compared to the matrix. For all melt sizes shown, the line scan also shows a slight decrease in the As and Ge content in the droplets suggesting that while the secondary (droplet) phase in 20 PbSe glasses are Pb-rich, the matrix phase is As and Ge-enriched and Pb-deficient as compared to the as-batched composition. The distribution of Pb in the XEDS map clearly matches with the TEM images (Figure 1A-C inset) where the bright and dark interfaces

correspond to the Pb-rich and Pb-deficient amorphous phases, respectively. In addition to the compositional information shown, the undulation in the line scans (and their breadth) illustrates the gradual boundary between the two phases. This differs from abrupt, step-like changes typically observed in droplet/matrix morphology, suggesting that the morphology is likely near a spinodal boundary. As described in Yadav et al.,[26] this is indeed the case as glasses in the same series comprised of ~25-35 mol% PbSe show spinodal morphology.

The results summarized in Figure 2A confirm that the atomic percentages of Ge, As, Pb and Se measured across numerous locations, show no variation with melt size, source of elemental starting materials, or melt protocol. These data suggest that the compositional uniformity of the glasses remains essentially constant with increasing melt size. TEM investigations of all samples exhibit LLPS, with Pb-rich droplets within a Pb-deficient matrix, however the average droplet diameter increases with increasing melt size as seen in Figure 2B. This shows that the thermodynamics of liquid-liquid immiscibility has an important bearing on
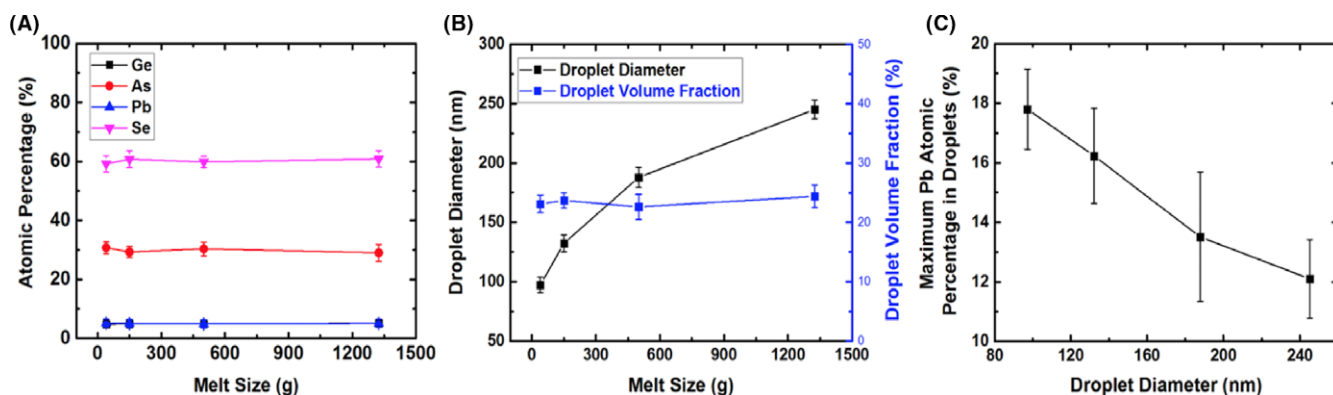

FIGURE 2 (A) Relationship between the atomic percentage of Ge, As, Pb and Se measured by EDS with melt size and plots of (B) the droplet diameter and volume fraction of droplets as a function of melt size and (C) the maximum Pb atomic percentage in droplets as a function of droplet diameter

the mechanism of phase separation as discussed in more detail elsewhere.[34,35] The size of the droplets in the larger melts produced at AMI (500 and 1325 g) is almost twice that of droplets seen in small melts (40 and 150 g), likely due to the very different (slower) quenching rates employed in the commercial melts. After phase separation initiates, the final size of the droplet diameter is affected by the thermodynamic driving force within the glass to reduce the interfacial free energy by minimizing the free surface area where the two phases contact each other. A glass cooled quickly through the critical temperature, can be expected to have smaller diameter droplets than the same melt cooled slowly. Examining the total volume fraction of droplets (a product of droplet size and number), one can see that the phase-separated droplets represents about 24% of the volume fraction of the glass and this fraction remains constant with melt size. This suggests that the thermodynamics of droplet formation is driven by the melt free energy, but the kinetics of the cooling process defines the number density of the secondary phase droplets. While the volume fraction of droplets remains nominally constant within the melts as shown in Figure 2B, the maximum Pb content (atomic percentage) in each droplet (Figure 2C) decreases as the droplet diameter increases. This observation is consistent with the increase in the droplet diameter discussed above.

In this study, different melt sizes represent different thermal histories (cooling rates from the melt) of glasses and a systematic progression from the most rapid (40 g melt size) to slowest (1325 g melt size) cooling rates. This variation in thermal history has a corresponding impact on the resulting glass' phase separated morphology and thermal properties. While the small size melts of 40 and 150 g were quenched by blowing compressed air on the ampoules, the 500 and 1325 g glasses were quenched by natural convection. As noted above, the difference (reduction) in cooling rate leads to an increase in droplet diameter with increasing melt size. The multiple amorphous phases formed as shown by TEM, can result in multiple glass transition temperature(s) as seen by differential scanning calorimetry (DSC).

As shown in the DSC spectra in Figure 3, signatures related to LLPS are readily visible. It has been reported previously that phase separation in glasses is often manifested by the presence of two glass transition temperatures, T_g's as measured by thermal analysis [36,37] which are associated with the amorphous phases present. However, such clear indication (multiple T_g's) may not always be observed in thermal analysis alone, and a secondary tool (ie, TEM) is usually employed to confirm definitively. Figure 3 shows DSC thermograms of glasses heated at 10°C/min for different melt size glasses. These spectra show features of two endothermic inflections before the onset of crystallization,
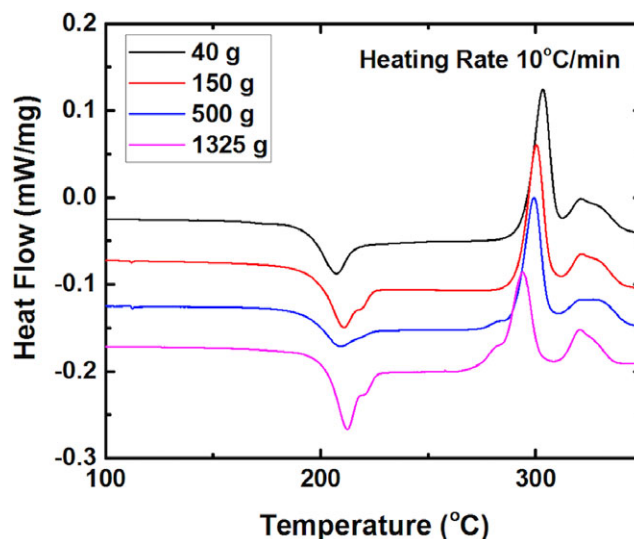

FIGURE 3 Results of conventional DSC curves for different melt size base glasses. Heating rate: 10°C/min

suggesting the existence of two glass transition temperatures. Not shown are the first derivatives of these curves where the subtle presence of the second T_g in the 500 g melt, is clearly evident. These features are followed by an exothermic crystallization peak which has been shown to be attributed to a Pb- and/or As-containing selenide crystal phase(s).[19] The presence of two glass transition temperatures is consistent with the phase separation as seen in TEM micrographs for all samples. While the two glass transition temperatures are clearly visible in samples from the 150, 500 and 1325 g melts, they cannot be seen in small melts such as the 40 g glass, likely due to the glass' higher cooling rate. The second T_g in the 40 g sample may be obscured because the volume fraction of this secondary glass phase is small and possibly possesses a composition more similar to the primary phase. The key thermal temperatures, as determined from the DSC data for all glasses are summarized in Table 1.

Table 1 compares the glass transition, thermal stability ($\Delta T = T_x - T_{g1}$) and crystallization temperatures (T_x, onset

TABLE 1 Characteristic temperatures obtained from DSC for four different melt size base glasses

Temperature (±2°C)	T_{g1} (°C)	T_{g2} (°C)	T_x (°C)	ΔT	T_{p1} (°C)	T_{p2} (°C)
Melt size						
40 g	202.5	–	294.5	92	303.3	321.0
150 g	206.6	217.2	291.8	85.2	300.9	320.8
500 g	204.2	216.1	287.8	83.6	298.8	321.2
1325 g	208.3	219.8	284.9	76.6	293.9	320.7

and T_p, peak) for glasses as the size of the melt is varied. As discussed earlier, with the exception of the 40 g sample, all glasses show two glass transition temperatures. As seen in the Figure 3 and Table 1, the onset of crystallization and first crystallization peak shifts toward the lower temperature as the melt size increases. This shift is believed to be associated with the different thermal histories of the glasses, and the likelihood of a higher concentration of quenched-in crystal nuclei with larger melt volumes prepared with more gradual cooling. This suggests that the slow-cooled melt(s) should contain more as-quenched nuclei than a more rapidly cooled melt because the slower quenching rate allows more time for crystal nuclei to potentially form. It can thus be expected that crystallization will occur in these samples at lower temperatures in the DSC because the preexisting crystal nuclei can start growing earlier in the thermal heating process. This fact is also reflected in the reduction in the glass' thermal stability with melt size, as defined by the calculated ΔT. It should be noted that the variation in thermal history does not lead to new peaks or shoulders in the DSC spectra which would be indicative of other species (nuclei) for potential crystallization. All glasses have one distinct crystallization peak followed by an asymmetric peak made of (at-least) two crystallization features. This is consistent with the phase formation discussed in the XRD analysis below. The 1325 g melt exhibited crystallization peaks, T_p at 293.9 and 320.7°C, whereas crystallization peaks for the same glass in 40 g size melts were seen at 303.3 and 321°C.

While the T_g of the all glasses are similar, the crystallization features for the glasses are different, suggestive that though the glasses crystallize similarly, the actual phase formation based on nuclei present, may vary. It is the analysis of this primary crystallization peak that has been used in the nucleation and growth rate determination experiments discussed below. The evolution of varying volume fractions of the same phases in the postheat-treated glass matrix, is in fact, realized as shown below.

Table 2 summarizes the variation in glass density, hardness and refractive index (as measured at $\lambda = 4.515$ μm) of the base glasses with melt size. As seen in the table there is little variation (within the measurement error shown) in these properties with melt size, a somewhat surprising finding given the extremely different thermal histories of the melts. These data suggest that the microscopic morphology variation discussed above imparted by the glass' thermal history variation, does not extend to the macroscopic scale over which these physical and optical properties are evaluated. In general, refractive index depends on the thermal history of the glass, which is of course, different according to the melt size. However, an appropriate annealing can also give the same thermal history for all glasses of different melt size, leading to the same refractive index. This is clearly not the case for the multiple melts evaluated here.

As mentioned earlier, the larger vessel and more controlled cooling conditions of the commercial glasses allows for better optical homogeneity. This is evident in Figure 4 which shows IR camera (transmission) images (through

TABLE 2 Melt size variation in density, hardness and refractive index (at 4.515 μm, 22°C) of the 20 PbSe base glass. Details on the measurement of density and hardness can be found in reference [23]

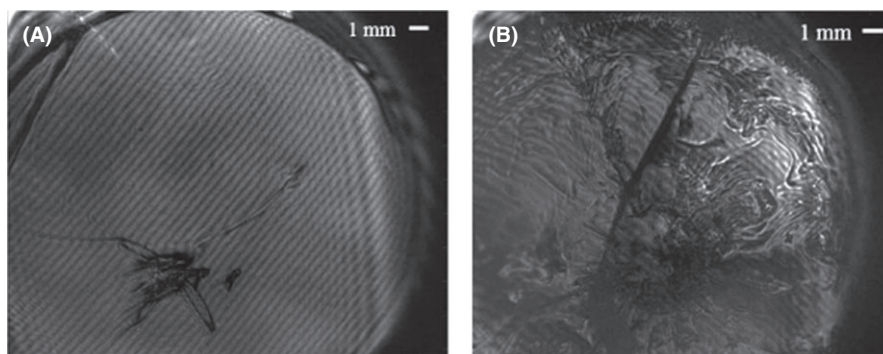| Melt size	40 g	150 g	500 g	1325 g
Properties				
Density (g/cm³)	4.978 ± 0.006	4.987 ± 0.009	4.998 ± 0.004	4.996 ± 0.002
Vickers hardness (MPa)	1715.78 ± 34.42	1641.13 ± 19.12	1689.55 ± 22.65	1646.94 ± 24.54
Refractive index at $\lambda = 4.515$ μm, 22°C	2.8440 ± 0.0002	2.8515 ± 0.0002	2.8471 ± 0.0002	2.8494 ± 0.0002

FIGURE 4 FLIR camera image of 20 PbSe melts: (A) AMI exploratory 1325 g melt sample (traditional melt/quench protocol); sample is 1" in diameter and 2.5 mm in thickness. B, Hand polished, 100 g UCF melt; sample is 30 mm in diameter and 2 mm in thickness

glass thicknesses of 2-2.5 mm) of the first exploratory large commercial melt produced as compared to the UCF small melt. An IR camera provides qualitative indications of defects but provides no quantitative measure of density or index variation. In Figure 4A, the exploratory commercial melt exhibits one large defect within a reasonably homogeneous slice. The quench/cooling method and large melting vessel's size greatly reduces the turbulent flow of the melt during the quench compared to the extremely aggressive lab scale melts which are quenched rapidly via active (forced air) cooling. The nonuniformity of such cooling gives rise to turbulence during the quench leading to the strong striae seen in small 100 g melt. Figure 5 illustrates the spatial variation in refractive index across a section of large (1325 g) and small (100 g) melt samples as measured in a Mach-Zehnder interferometer system (λ = 4.5905 µm) at the University of Rochester.

As qualitatively shown in Figures 4 and 5 quantitatively reflects the impact of melt size on measured refractive index and optical homogeneity. The result of the AMI glass' slower quenching yields a much more uniform refractive index map as compared to the small melt which shows the variation in index that accompanies the density variations related to striae. While the magnitude of index variation is still large for precision optical applications (which typically dictate a refractive index homogeneity of Δn of $\sim10^{-4}$ or better), the spatial comparison of index uniformity between such radically different thermal history is noted. These data provide a much clearer representation of the significant density fluctuations caused by the turbulent melt conditions during the lab-scale melt's quench. The index map shows extremely good index uniformity in 1325 g glass except around the shown defect, with a nominal homogeneity (excluding the striae) of $\sim1.5 \times 10^{-4}$. This is compared to the small melt variation which is one

order of magnitude less ($\sim1 \times 10^{-3}$), illustrating the impact of the rapid quench protocol used.

Figure 6 shows the transmission spectra of the 20 PbSe glasses for melts ranging from 40 to 1325 g in size. We define the limits of the transmission window as 90% of the maximum transmission. Small 40 g and 150 g melts were found to have a short wavelength band-edge at 1.82 and 2.132 µm, respectively. The short-wave transmission edge for 500 and 1325 g melts were found to be at 4.00 and 3.54 µm respectively. The shape of the short wavelength edge of the glass provides insight into the magnitude of the scattering loss induced by the droplets (their size and index) and the index variation (difference) between the two amorphous phases. While the glass remains amorphous, the size of the droplets impacts the sharpness (steepness) of the short wavelength edge shown in the FTIR spectra. The red shift in large melt size is likely due to the fact that melts of 500 and 1325 g size were cooled more slowly leading to larger, as-quenched droplets of the secondary, amorphous phase as seen in TEM images of Figure 1. This is perhaps the most important aspect of the scale-up protocol to create high homogeneity, low (absorption + scatter) loss optical glass, and the challenges of traditional melt-quench protocols.

3.2 | Glass-ceramic properties as a function of melt size

Nucleation-like and growth-like curves provide information on the relative rates of nucleation and growth of crystals in the glass matrix as a function of temperature, but do not give absolute values of rates. To identify heat treatment protocols that will yield "optimal" microstructures suitable for optical applications, it is important to understand the temperature regimes and rates for nucleation and growth in
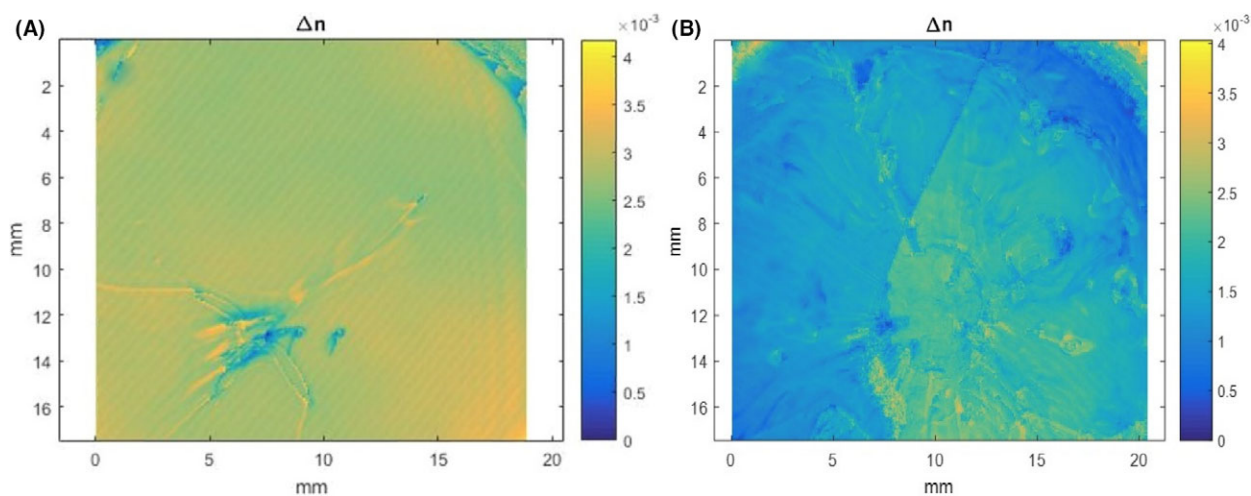

FIGURE 5 Large area refractive index homogeneity map (measured at λ = 4.5905 µm for a sample from an exploratory commercial scale AMI 1325 g melt (A) and a lab-scale 100 g melt (B) prepared at UCF
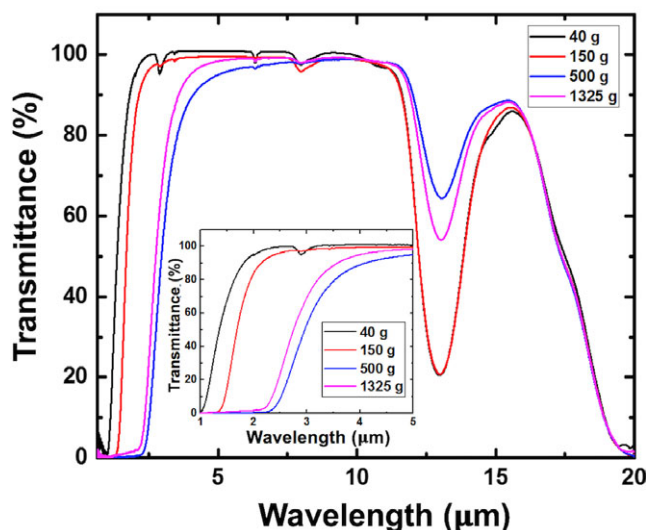
FIGURE 6 FTIR spectra of the base glasses with the melt size. Spectra are corrected for thickness and Fresnel losses

order to control the number and size of crystals in the glass matrix. These quantitative data can then be used to define the suitable temperatures and times for heat treatments used to generate crystals with controlled number density (defined by the nucleation step) and final size (defined in the growth step). Ideally, a theoretical model material for controlled crystallization would exhibit well-separated nucleation-like and growth-like curves. If the nucleation and growth rate curves overlap in temperature space, heat treatments in the overlap region lead to a broader size distribution of crystallites, as early nuclei grow while new nuclei form. Good separation of the two rate curves allows for the implementation of a two-step heat treatment where the first step nucleates crystals in the matrix without appreciable crystal growth and the second step grows the previously nucleated crystals without creating additional nuclei. This two-step heat treatment procedure typically yields crystals with a narrow size distribution, desirable in optical glass ceramics.

Nucleation-like and growth-like curves were determined for the four (4) melts examined in our study. The variation in these rate curves with temperature are shown in Figure 7. Figure 7A and B, highlight the variation in curve separation between the largest (1325 g) and smallest (40 g) melt. As one might expect, the slower cooling rate of the large melt reduces the separation between the nucleation and growth curves as compared to the smaller, more rapidly quenched 40 g melt volume. While the onset temperature of the nucleation curve shows little difference (despite a possible variation in the number density (higher) of quenched-in nuclei in the larger melt), the presence of these nuclei are noted in the earlier onset temperature for
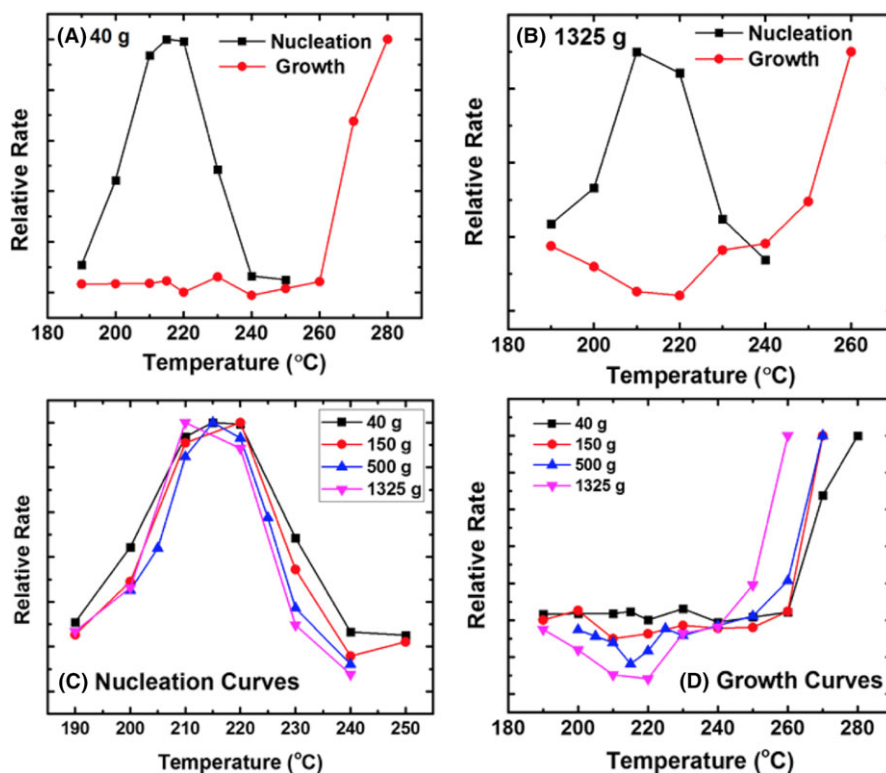

FIGURE 7 Nucleation-like and growth-like curves for the 40 g melt (A) and 1325 g melt (B); comparison of the location of the temperature maxima of nucleation (C) and growth curves (D) for 20 PbSe glasses as a function of melt size

crystal growth in Figure 7B. A measurable increase in growth rate not present until after 260°C for the small melt, occurs earlier (near 240°C) in the large melt. This is likely due to a larger concentration of as-quench nuclei present in the larger melt, which can initiate growth sooner, at a lower temperature. The positions of both peak rates and onset temperatures are extremely important as they are used to define the heat treatment protocols used to create glass-ceramic. As seen in Figure 7C, the nucleation regime for all glasses starts near 190°C, exhibit a maximum nucleation rate in the 210–220°C range, which then decreases back to near zero at 240°C. The variation in growth rate with melt size can clearly be seen in Figure 7D. The onset temperature in each melt's growth rate curve shifts to higher temperatures as melt size is reduced. This variation can likely be correlated with fewer growth sites (nuclei) in smaller, more rapidly cooled melts.

Figure 7 also illustrates a clear separation between the nucleation-like and growth-like curves, an aspect that is desirable for making glass-ceramics based on a thermally separated, two-step heat treatment protocol. As the growth regime doesn't begin until ~20-25°C after the nucleation regime ends, this separation defines the material's 'process window', the regime where no (or few) new nuclei should form while the existing nuclei will grow. This is a desirable attribute because for optical applications a narrow size distribution of crystallites ensure a lower level of scatter. The process window data was used to define the referenced two step time/temperature regime used on for all melts. The nucleation heat treatment was chosen to be at the maximum nucleation rate where zero growth rate was seen. For all melt size glasses nucleation was performed at 220°C for 2 hours while three (different) growth heat treatments were investigated for 30 minutes at temperatures of 250, 260 or

270°C. These three temperatures were chosen to examine the extent of crystallization and the formation of possible (multiple) crystal phases that might form (as suggested in the DSC data) with varying growth rates. Note that the growth-like curve determination protocol was only applied to the most intense, lowest temperature crystallization peak in the DSC spectra. Hence, growth rates are really only indicative of that specific phase's crystallization behavior, a limitation of analysis if we expect multiple crystal phases to form as we do here. Figure 7C and D clearly illustrate the effect of changing melt size on nucleation and growth rate curves for the 20 PbSe composition.

Figure 8A and E show representative high resolution BF TEM images collected from 40 and 1325 g samples, heat treated with a growth protocol of 30 minutes at 270°C where secondary phases with crystalline fringes are observed to be embedded in an amorphous matrix. The glass-ceramic nanocomposite morphology is further confirmed by corresponding SAED patterns collected from the entire region in Figure 8A and E which illustrate the co-existence of crystalline spots and diffuse rings, as shown in Figure 8B and F, respectively. To identify the type of crystalline phases, interplanar spacings were extracted from local regions in Figure 8A and E (highlighted by the dotted squares), as shown in Figure 8C and G, respectively. Figure 8D and H shows corresponding FFT images which were subsequently collected from the image in Figure 8C and D to identify the lattice symmetries of the crystals, respectively. The extracted interplanar spacing of ~3Å with their cubic lattice symmetries closely match the reported value for {200} planes of crystalline PbSe,[38] indicating the heat treatment-induced crystallization of Pb-rich secondary phases in parent base samples and the resulting growth of PbSe nanocrystals. While this is not the only crystal phase
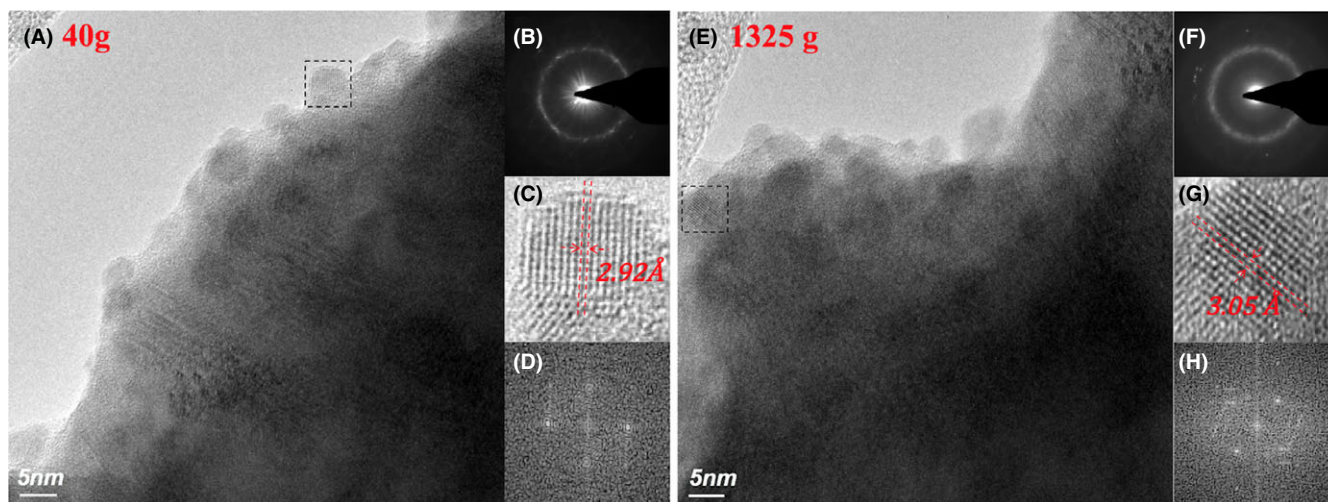

FIGURE 8 Bright field transmission electron microscope (BF TEM) images, selected area electron diffraction (SAED) patterns, enlarged images of crystals, and fast Fourier transform (FFT) images for 40 g (A-D) and 1325 g (E-H) melt size glass-ceramics upon nucleation and growth heat treatment for 30 minutes at 270°C

formed upon heat treatment, it is the dominant PbSe high index (n ~ 4 in the IR) phase that will have the largest contribution to the glass ceramic's increase in effective refractive index.

On the basis of TEM results (Figure 8), XRD scans were carried out to identify and confirm the crystallizing phases in the glassy matrix resulting from the noted heat treatment protocol. XRD was performed on bulk samples from all the nucleated (220°C-2 hours) and growth heat treatments of 260 and 270°C in order to identify the precipitating crystal phase(s) and to see at what temperature, detectable crystallization occurs. At the very early stages of heat treatment for the nucleation + 250°C-30 minutes samples, no signs of crystalline phase formation can be observed. Figure 9 shows the overlay of the base glass, nucleation + 260°C-30 minutes, and nucleation + 270°C-30 minutes samples. The nucleation + 260°C-30 minutes spectra look very similar to the base curve, but has new crystal peaks at 2θ values of approximately 18, 30, 31, and 31.5°. The peaks after nucleation + 260°C-30 minutes are more clearly defined in the 1325 g melt as compared to the 40 g sample, likely because of the earlier onset of the crystal growth suggested in data in Figure 7D. Both samples that underwent the higher temperature growth treatment at 270°C revealed crystal peaks after heat treatment exhibiting a more crystallized, higher volume fraction than the lower heat treatment temperature samples. What is important for our scale-up comparison is that the same phases are clearly evident but evolve at different rates, consistent with inferences predicted in the nucleation and growth rate data.

Key observations of phase evolution differences related to melt size, while present, are minor. Crystal phases formed in both melts are the same, with minor variations in phase fraction(s) estimated by examining peak intensities. Comparing the fractions of desirable high- index crystal phases (PbSe - pink cross, and $Ge_{0.1}(PbSe)_{0.9}$ - orange circle) within the lower index glassy phases that define the nanocomposite's index modification as compared to the parent glass, one might infer a minor variation (increase) in these phases in the larger melt as compared to the smaller melt size. Perhaps more impactful to the nanocomposite's resulting index after heat treatment, the 40 g melt can be seen to have a slightly higher fraction of As-Se phases (As_2Se_3 - blue stars, and AsSe - green diamonds). Since the refractive index of these crystals are very similar to that of the parent glass, their formation and presence has little to no impact on any increase in the nanocomposite's resulting effective index, a primary goal of our GRIN application. These qualitative observations of the XRD data, are validated in the λ = 4.515 μm refractive index data shown below.

As shown in Figure 10, the material's refractive index is significantly impacted by the various heat treatments used. The density values shown for all as-melted glasses in Table 2, exhibit thermal history related variation, whereby slower cooled glasses have a smaller molar volume, and thus, higher density. This effect extends to the index property for other base glass samples, regardless of melt size. As seen in Figure 10, the refractive index at 4.515 μm of the heat-treated materials (depicted in Figure 10 for the small 40 g and largest 1325 g melts only), decreases from 2.8440 to 2.8309 for 40 g and from 2.8494 to 2.8404 for 1325 g melt size after the nucleation heat treatment. The subsequent growth heat treatments at 250, 260, and 270°C increase the refractive index up to 2.8723 and 2.8925 for 40 and 1325 g, respectively. The initial decrease in index with nucleation is likely caused by additional changes in the extent of phase separation and has been observed across the GAP-Se series. This changes the composition of the residual glass, which then participates in crystallization, during the heat treatment processes. The subsequent increase in index is caused by the growth of Pb-containing crystals with higher refractive index to the point where their volume fraction becomes significant. Eventually, the Pb available to participate in formation of the high index phase(s) will be depleted and any further increase in index
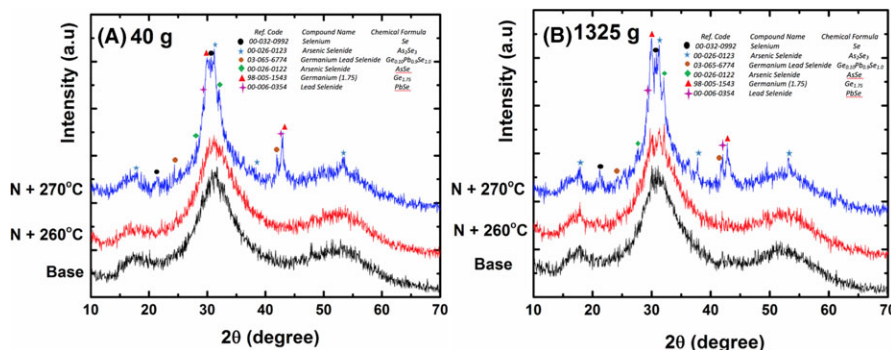

FIGURE 9 XRD patterns of selected melts (A) 40 g and (B) 1325 g following nucleation and growth heat treatment at 250, 260, and 270°C
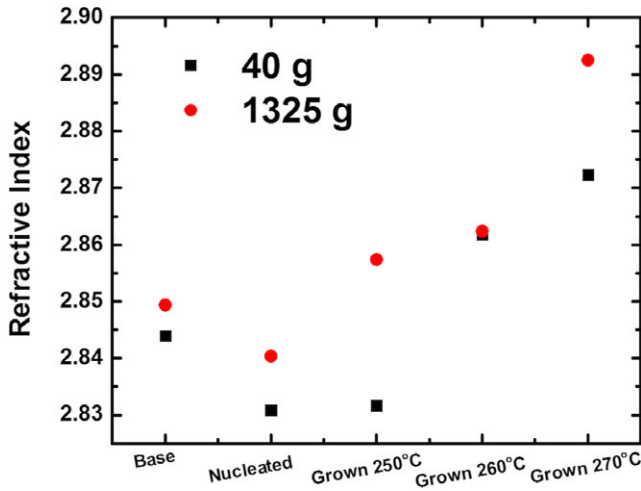
FIGURE 10 Change in refractive index measured at λ = 4.515 μm after heat treatment for 40 and 1325 g melts. Error is within the size of the data points

would be expected to saturate. While this has been observed in higher Pb-content (40 PbSe) thin films[39] where laser exposure was used to nucleate the high index phase (followed by a homogeneous growth step), no indication of saturation is seen under the heat treatment conditions employed here. This concurrent process of low and high refractive index phase formation of varying crystal phases is also reflected in the postheat-treated glass-ceramic's transmission, and substantiated by the XRD data presented.

Figure 11 shows the transmittance spectra of the base and heat-treated glass-ceramic composites for the 40 and 1325 g melts. The nucleation step slightly red-shifts the cutoff but the slight increase in phase separation noted above for both large and small melt sizes, does not adversely affect transmission. Further heat treatment to form a glass ceramic changes the refractive index of 20 PbSe glass and also causes the short wavelength edge to shift to higher wavelengths, due to an increase in scattering associated with nanocrystal phase formation. This scattering

is more pronounced for large melts where preheat treatment droplet size is larger but lower in Pb content. Here the index difference between amorphous phases is small, as compared to the large index contrast in the many small droplets found in small melts. Thus, it can be surmised that the scatter's size, rather than index difference is defining the scatter. The subsequent growth heat treatments increase the presence of high index PbSe containing phases (as well as some similar index crystalline As_2Se_3 and Se phases). While these crystallites have indices similar to surrounding parent glass they do not appreciably contribute to the effective refractive index change, but they do have a role in reducing transmission by scattering, due to their presence. Growth at 270°C noticeably shifts the cutoff to higher wavelengths with a large change in index (due to more low and high index phases formed). While these growth temperatures show significant increases in the resulting effective refractive index change (dictated by the volume fraction of high index nanocrystals in the remaining depleted glassy matrix), the corresponding loss in transmission is unacceptable for the target application. Adjustments to the growth protocols, as suggested by use of lower growth temperatures are expected to be able to produce a higher number density of crystals of a smaller size as suggested by the 250°C heat treatment curves shown. Most clearly evident is that the large number density of small size, high Pb-content droplets present in the small melts allow preservation of transmission at the expense of postheat treatment index change. Hence, further optimization beyond that used in this study, would likely lead to an acceptable, intermediate magnitude change in index, with an acceptable MWIR transmission window.

4 | CONCLUSIONS

A series of $20GeSe_2$-$60As_2Se_3$-$20PbSe$ (20 PbSe) GAP-Se chalcogenide glasses of varying melt size were prepared and characterized. Melt size spans small, lab-scale (40 g) up to
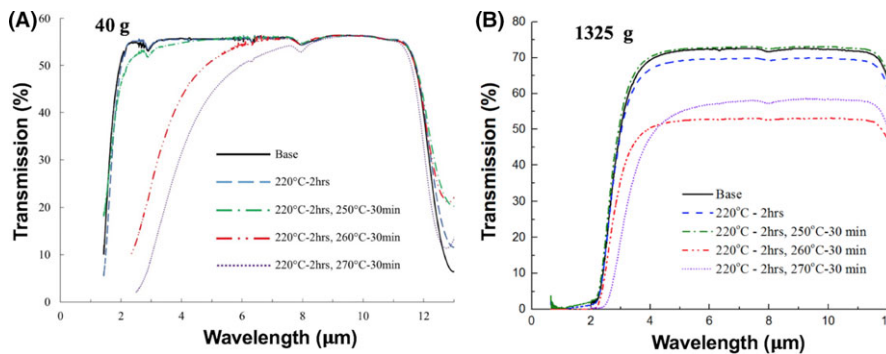

FIGURE 11 FTIR transmission spectra of base and heat treated (A) 40 g (B) and 1325 g 20 PbSe glass. Sample thickness normalized to 2 mm. Not corrected for Fresnel loss

commercially relevant melt sizes (1.325 kg), and due to this variation in size and melt protocol, exhibit vastly different thermal histories. Samples were evaluated to examine and quantify the effect of these processing variables on starting glass morphology (LLPS) and as-melted physical and optical properties. Optical and physical property variation was shown to be directly related to thermal history as evidenced by thermal and microscopic evaluation. Two glass-transition temperatures were observed for three of the four examined glasses and the size and composition of amorphous, Pb-rich droplets in the TEM images illustrate the role of cooling rate and melt size, on droplet morphology. No variation in total droplet volume fraction was observed, however droplet size directly correlated with melt size. Small melts were shown to have a larger number of smaller, high Pb-content droplets and droplet Pb content decreased with increasing droplet and melt size. While minimal variation in density, hardness and refractive index of base glass was observed with varying melt size, melt size and thermal history was shown to largely influence the short wavelength transmission edge due to the scattering contribution imparted by the secondary, high index droplet phase. Cooling rate was also shown to have a significant effect on the presence of striae and the melt's refractive index uniformity, quantified for small (1.5×10^{-3}) and large melts (5×10^{-4}).

Nucleation- and growth-like curves were generated for glass from each of the four melt sizes. In evaluating the key temperatures (temperature at which the rates are maximum, breadth of the rate curves) it was shown that melt size does not impact the 20 PbSe melt nucleation rate but the thermal history variation does impart a measurable variation on growth rates. Specifically, the onset of growth rate curves shows an expected variation where the onset temperature is lowest in larger melts likely due to the number of as-quenched nuclei which would be expected to be larger in slower cooled melts. Temperatures extracted from the nucleation and growth-like curves were used to define a fixed, two-step heat treatment protocol which was applied to all glasses to quantify the impact on resulting glass-ceramic property variation. Following heat treatment, refractive index shows significant changes associated with the formation of higher index crystalline phases. The increase in effective refractive index, n_{eff}, after the heat treatment can be directly correlated with the growth of Pb-rich crystal phases in the composite which form along with other phases, which have indices close to that of the parent glass thereby not influencing the resulting composite's index. Crystal phases were identified by TEM and XRD confirming formation of higher index, PbSe containing phase(s) within the Pb-deficient matrix. Qualitative evaluation from XRD and TEM of fraction of crystal phases showed little variation in volume fractions of crystal phase between the largest and smaller melt sizes, though crystallization was found to be dominant within the initially formed, Pb-rich droplets.

These findings provide experimental evidence for the variation in melt morphology and nanocomposite microstructure with melt size, and the corresponding effect in chalcogenide glass-ceramics at the micro-scale. The suitability of using lab-scale data to predict the success of commercial scale up has been confirmed, and thus suggests how such experiments can be used to predict relevant optical and physical properties prior to initiating large-scale manufacturing of exploratory melts. Such findings are useful in directly comparing the tradeoff's related to manufacturing of components for IR GRIN applications, as summarized in the recent review.[40]

ACKNOWLEDGMENTS

ORCID

Anupama Yadav http://orcid.org/0000-0002-3766-7082

REFERENCES

1. Zakery A, Elliott SR. Optical properties and applications of chalcogenide glasses: a review. J Non-Cryst Solids. 2003;330(1–3):1–2.

2. Quémard C, Smektala F, Couderc V, Barthelemy A, Lucas J. Chalcogenide glasses with high nonlinear optical properties for telecommunications. J Phys Chem Solids. 2001;62(8):1435–40.

3. Zhang XH, Calvez L, Seznec V, Ma HL, Danto S, Houizot P, et al. Infrared transmitting glasses and glass-ceramics. J Non-Cryst Solids. 2006;352(23–25):2411–5.

4. Seddon AB. Chalcogenide glasses: a review of their preparation, properties and applications. J Non-Cryst Solids. 1995;184:44–50.

5. Dantanarayana HG, Abdel-Moneim N, Tang Z, Sojka L, Sujecki S, Furniss D, et al. Refractive index dispersion of chalcogenide glasses for ultra-high numerical aperture fiber for mid-infrared supercontinuum generation. Opt Mater Express. 2014;4(7):1444–55.

6. Cha DH, Kim HJ, Hwang Y, Jeong JC, Kim JH. Fabrication of molded chalcogenide-glass lens for thermal imaging applications. Appl Opt. 2012;51(23):5649–56.

7. Sanghera JS, Shaw LB, Aggarwal ID. Chalcogenide glass-fiber-based mid-IR sources and applications. IEEE J Sel Top Quantum Electron. 2009;15(1):114–9.

8. Mao X, Lin SC, Lapsley MI, Shi J, Juluri BK, Huang TJ. Tunable Liquid Gradient Refractive Index (L-GRIN) lens with two degrees of freedom. Lab Chip. 2009;9(14):2050–8.

9. Fantone SD. Refractive index and spectral models for gradient-index materials. Appl Opt. 1983;22(3):432–40.

10. Wu Q, Turpin JP, Werner DH. Integrated photonic systems based on transformation optics enabled gradient index devices. Light Sci Appl. 2012;1(11):e38.

11. Moore DT. Gradient-index optics: a review. Appl Opt. 1980;19(7):1035–8.

12. Visconti AJ, Fang K, Corsetti JA, McCarthy P, Schmidt GR, Moore DT. Design and fabrication of a polymer gradient-index optical element for a high-performance eyepiece. Opt Eng. 2013;52(11):112107.

13. Pickering MA, Taylor RL, Moore DT. Gradient infrared optical material prepared by a chemical vapor deposition process. Appl Opt. 1986;25(19):3364–72.

14. Ohmi S, Sakai H, Asahara Y, Nakayama S, Yoneda Y, Izumitani T. Gradient-index rod lens made by a double ion-exchange process. Appl Opt. 1988;27(3):496–9.

15. Nag N, Jha S, Sastri S, Goldman LM, McCarthy P, Schmidt GR, et al. ALON GRIN optics for visible-MWIR applications. Proceedings of SPIE Defense + Security, Advanced Optics for Defense Applications: UV through LWIR; 2016, Baltimore, USA. Vol. 9822, p. 98220V.

16. Sinai P. Correction of optical aberrations by neutron irradiation. Appl Opt. 1971;10(1):99–104.

17. Gibson D, Bayya S, Nguyen V, Sanghera J, Kotov M, McClain C, et al. IR GRIN optics: design and fabrication. Proceedings of SPIE Defense + Security, Advanced Optics for Defense Applications: UV through LWIR II; 2017, Orlando, USA. Vol. 10181, p. 101810B.

18. Hensler JR, inventor; Bausch, Lomb Inc, assignee. Method of producing a refractive index gradient in glass. United States patent US 3,873,408. 1975 Mar 25.

19. Corsetti JA, Moore DT. Design of a ZnS/ZnSe radial gradient-index objective lens in the mid-wave infrared. Proceedings of Optical Society of America, Imaging Systems and Applications; 2013, p. ITu2E-3.

20. Mayer T, Werner D, Rivero-Baleine C, Richardson K. Innovative design and manufacturing of gradient-index-based transformation optics components. DARPA Manufacturable Gradient Index Optics Program (MGRIN), Contract Number FA8650-12-C-7225. 2012.

21. Ji-jian C. Microstructure and properties of selenide glasses after controlled crystallization. J Non-Cryst Solids. 1983;56(1–3):303–8.

22. Song SM, Choi SY, Lee YK. Crystallization property effects in $Ge_{30}Se_{60}Te_{10}$ glass. J Non-Cryst Solids. 1997;217(1):79–82.

23. Buff A. A study of crystallization behavior in phase separated chalcogenide glasses. MS Thesis, University of Central Florida; 2016.

24. Mecholsky JJ, Srinivasan GR, Moynihan CT, Macedo PB. Immiscibility and liquidus temperatures in the pseudobinary chalcogenide system $PbSeGe_{1.5}As_{0.5}Se_3$. J Non-Cryst Solids. 1973;11(4):331–40.

25. Varshneya AK. *Fundamentals of inorganic glasses*. New York City, NY: Elsevier; 2013.

26. Yadav A, Kang M, Smith C, Lonergan J, Buff A, Sisken L, et al. Influence of phase separation on structure–property relationships in the $(GeSe_2–3As_2Se_3)_{1-x}$ $PbSe_x$ glass system. Phys Chem Glasses-Eur J Glass Sci Technol Part B. 2017;58(4):115–26.

27. Marotta A, Buri A, Branda F. Nucleation in glass and differential thermal analysis. J Mater Sci. 1981;16(2):341–4.

28. Ray CS, Ranasinghe KS, Day DE. Determining crystal growth rate-type of curves in glasses by differential thermal analysis. Solid State Sci. 2001;3(6):727–32.

29. Carlie N, Anheier NC Jr, Qiao HA, Bernacki B, Phillips MC, Petit L, et al. Measurement of the refractive index dispersion of As2Se3 bulk glass and thin films prior to and after laser irradiation and annealing using prism coupling in the near-and mid-infrared spectral range. Rev Sci Instrum. 2011;82(5):053103.

30. Qiao HA, Anheier NC, Musgrave JD, Richardson K, Hewak DW. Measurement of chalcogenide glass optical dispersion using a mid-infrared prism coupler. Proceedings of SPIE Defense Security and Sensing, Window and Dome Technologies and Materials XII; 2011, Orlando, USA. Vol. 8016, p. 80160F.

31. Gleason B, Richardson K, Sisken L, Smith C. Refractive Index and Thermo-Optic Coefficients of Ge-As-Se Chalcogenide Glasses. Int J Appl Glass Sci. 2016;7(3):374–83.

32. Zhao Y. Low-coherence interferometer for dimensional metrology. PhD Thesis, University of Rochester; 2018.

33. Yee AJ, Moore DT. Free-space infrared Mach-Zehnder interferometer for relative index of refraction measurement of gradient index optics. Opt Eng. 2017;56(11):111707.

34. Shelby JE. Introduction to glass science and technology. Royal Society of Chemistry; 2005.

35. James PF. Liquid-phase separation in glass-forming systems. J Mater Sci. 1975;10(10):1802–25.

36. Goel A, Tulyaganov DU, Goel IK, Shaaban ER, Ferreira JM. Effect of BaO on the crystallization kinetics of glasses along the Diopside–Ca-Tschermak join. J Non-Cryst Solids. 2009;355(3):193–202.

37. Moynihan CT, Macedo PB, Aggarwal ID, Schnaus UE. Direct observation of the double glass transition in a phase-separated glass. J Non-Cryst Solids. 1971;6(4):322–8.

38. Dalven R. A review of the semiconductor properties of PbTe, PbSe. PbS PbO Infrared Phys. 1969;9(4):141–84.

39. Kang M, Swisher AM, Pogrebnyakov AV, Liu L, Kirk A, Aiken S, et al. Ultra-low dispersion multicomponent thin film chalcogenide glass for broadband gradient index optics. Adv. Mater. 2018;30, 1803628. DOI: 10.1002/adma.201803628.

40. Richardson K, Kang M, Sisken L, Yadav A, Blanco C, Antia M, et al. Advances in infrared GRIN: a review of novel materials towards components and devices. Proceedings of SPIE Defense + Security, Advanced Optics for Defense Applications: UV through LWIR III; 2018, Orlando, USA. Vol. 10627, p. 106270A.